TURBULENT VISCOPLASTIC FLOWS INSIDE A LID-DRIVEN CAVITY

Paulo Arthur Beck, 00080322@ufrgs.br
Horacio Antônio Vielmo, vielmoh@mecanica.ufrgs.br
Sergio Luiz Frey, frey@mecanica.ufrgs.br
Department of Mechanical Engineering, Federal University of Rio Grande do Sul (UFRGS),
Rua Sarmento Leite 425, 90050-170, Porto Alegre, RS, Brazil.

Abstract. *This paper presents the results obtained by numerically simulating lid-driven flows of a viscoplastic liquid inside a 3D cavity. The flows are formulated by the principles of mass and momentum balances and the V2F k-epsilon turbulence model equations. The liquid's dynamic viscosity is given by the SMD viscosity function such that the shear stress field is regularized using only rheological properties. The Finite Volume Method is applied to linearize the system of transport equations characterizing the flows. The problem domain is discretized by hexahedral volumes and the resulting meshes are verified following the generalized Richardson's Extrapolation Method. The effects of inertia and turbulence on the flow's morphology and yield surfaces are presented for a fixed set of governing parameters and varying power-law Reynolds numbers.*

Keywords*: Viscoplasticity, SMD Viscosity Function, Turbulence, V2F k-epsilon Model*

1. INTRODUCTION

This paper presents the results obtained by numerically simulating lid-driven flows of a viscoplastic non-Newtonian liquid inside a 3D cavity. The incompressible Navier-Stokes transport equations and the $k-\varepsilon-\overline{\vartheta^2}$ (V2F *k*-epsilon) turbulence model equations formulate the flows. The SMD viscosity function models the liquid's dynamic viscosity. After verification of the suitability of the meshes used to simulate the flows, the authors analyze the effects on the morphology of the yield stress and vorticity fields when the flow transitions from the laminar to the turbulent regime for a fixed set of governing parameters.

2. MODELING

Equations (1) and (2) give the integral formulation of the Navier-Stokes equations for continuity and momentum:

$$\frac{d}{dt}\int_V \rho dV + \oint_A \rho \mathbf{u}\cdot\mathbf{da} = 0, \tag{1}$$

$$\frac{d}{dt}\int_V \rho \mathbf{u} dV + \oint_A \rho \mathbf{u}\otimes\mathbf{u}\cdot\mathbf{da} = -\oint_A p\mathbf{I}\cdot\mathbf{da} + \oint_A \mathbf{T}\cdot\mathbf{da} + \int_V \mathbf{f} dV. \tag{2}$$

In the preceding equations, ρ is the density, **da** is an infinitesimal area vector, dV is an infinitesimal volume, p is the hydrostatic pressure, **f** is the resultant of the body forces and **u** is the velocity vector. In Eq. (2), the terms on the left-hand side are the transient term and the convective flux. On the right-hand side are the pressure gradient term, the viscous flux and the body force term. **I** is the identity tensor and **T** is the viscous stress tensor. For a mean flow with an eddy viscosity, the Boussinesq approximation models the viscous stress tensor such that

$$\mathbf{T} = (\mu+\mu_t)\left[\nabla\mathbf{u} + \nabla\mathbf{u}^{\mathrm{T}} - \frac{2}{3}(\nabla\cdot\mathbf{u})\mathbf{I}\right]. \tag{3}$$

In Eq. (3), μ is the dynamic viscosity and μ_t is the eddy viscosity. To evaluate the later, the V2F *k*-epsilon turbulence model is used. According to Durbin (1995), the model captures near-wall effects more accurately by not relying on wall distance or damping functions. The model's transport equations (4) to (7) below solve the turbulence kinetic energy *k*, the dissipation rate ε and two additional turbulence quantities, namely the normal stress function $\overline{\vartheta^2}$ and the elliptic function *f*:

$$\frac{d}{dt}\int_V \rho k dV + \oint_A \rho k\mathbf{u}\cdot\mathbf{da} = \oint_A \left(\mu+\frac{\mu_t}{\sigma_k}\right)\nabla k\cdot\mathbf{da} + \int_V (G_k-\rho\varepsilon)dV\,, \tag{4}$$

$$\frac{d}{dt}\int_V \rho\varepsilon dV + \oint_A \rho\varepsilon\mathbf{u}\cdot\mathbf{da} = \oint_A \left(\mu + \frac{\mu_t}{\sigma_\varepsilon}\right)\nabla k\cdot\mathbf{da} + \int_V \left[\rho S^2 C_{\varepsilon 1} C_\mu\left(\overline{\vartheta^2} + a\sqrt{\vartheta^2}k\right) - (C_{\varepsilon 2}\rho\varepsilon/T)\right]dV\,, \tag{5}$$

$$\begin{aligned}\frac{d}{dt}\int_V \rho\overline{\vartheta^2}dV + \oint_A \rho\overline{\vartheta^2}\mathbf{u}\cdot\mathbf{da} \\ = \oint_A \left(\mu + \frac{\mu_t}{\sigma_k}\right)\nabla\overline{\vartheta^2}\cdot\mathbf{da} \\ + \int_V \left[\rho min\left\{kf, -\frac{1}{T}\left[(C_1-6)\overline{\vartheta^2} - \frac{2k}{3}(C_1-1)\right] + C_2 G_k\right\} - \frac{6\rho\overline{\vartheta^2}\varepsilon}{k}\right]dV\,,\end{aligned} \tag{6}$$

$$\int_A L^2\nabla f\cdot\mathbf{da} + \int_V \left[-f + \frac{1}{T}(C_1-1)\left(\frac{2}{3} - \frac{\overline{\vartheta^2}}{k}\right) + C_2\frac{C_\mu\overline{\vartheta^2}S^2}{\varepsilon} + \frac{5\overline{\vartheta^2}}{kT}\right]dV = 0. \tag{7}$$

In the above equations, the turbulence production term G_k has the same definition as in the standard *k*-ε model (Jones and Launder, 1972) where

$$G_k = \mu_t S^2 - \frac{2}{3}\rho k\nabla\cdot\mathbf{u} - \frac{2}{3}\mu_t(\nabla\cdot\mathbf{u})^2. \tag{8}$$

The modulus of the mean strain rate tensor is given by $S = |\mathbf{S}| = \sqrt{2\mathbf{S}:\mathbf{S}^{\mathrm{T}}}$ where $\mathbf{S} = 1/2\,(\nabla\mathbf{u} + \nabla\mathbf{u}^{\mathrm{T}})$. Equation (9) gives the realizable turbulent time scale:

$$T = min\left(\max\left(\frac{k}{\varepsilon}, C_t\sqrt{\frac{\nu}{\varepsilon}}\right), \frac{\alpha k}{C_\mu\overline{\vartheta^2}S\sqrt{3}}\right). \tag{9}$$

Equation (10) defines the turbulent length scale as

$$L = C_L max\left(\min\left(\frac{k^{3/2}}{\varepsilon}, \frac{k^{3/2}}{C_\mu\overline{\vartheta^2}S\sqrt{3}}\right), C_\eta\left(\frac{\nu^3}{\varepsilon}\right)^{1/4}\right). \tag{10}$$

The eddy viscosity μ_t computes as

$$\mu_t = \rho T_{min}\left(C_{\mu_{std}}k, C_{\mu_{\vartheta^2}}\vartheta^2\right). \tag{11}$$

In all previous equations, ν represents the kinematic viscosity. The model's coefficients are:

$$\begin{aligned}&a = 0.045, \alpha = 0.6, C_{\varepsilon 1} = 1.4, C_{\varepsilon 2} = 1.9, C_{\mu_{std}} = 0.09, C_{\mu_{\vartheta^2}} = 0.22, \sigma_k = 1.0, \sigma_\varepsilon = 1.3, C_1 = 1.4,\\ &C_2 = 0.3, C_\eta = 70.0, C_t = 6.0, C_L = 0.23.\end{aligned} \tag{12}$$

The liquid's dynamic viscosity μ is given by the SMD viscosity function (de Souza Mendes and Dutra, 2004). The function takes the flow's strain rate $\dot{\gamma}$ and the liquid's rheological properties as arguments such that

$$\mu = \mu(\dot{\gamma}) = \left(1 - e^{\frac{-\mu_0\dot{\gamma}}{\tau_0}}\right)\left(\frac{\tau_0}{\dot{\gamma}} + K\dot{\gamma}^{n-1}\right). \tag{13}$$

In Eq. (13), $\dot{\gamma} \equiv S$ is the modulus of the mean strain rate tensor. The liquid's zero-shear-rate viscosity and yield stress limit are μ_0 and τ_0 respectively. The power-law coefficient *n* controls the viscosity shear thinning beyond the liquid's yield stress limit. *K* is the consistency index and μ_0/τ_0 is a regularized rheological parameter that controls both the yield stress and the power-law terms of the equation. Figure 1 is a plot of the SMD viscosity function for *K* = 1 Pa·s$^{0.5}$, *n* = 0.5, μ_0 = 1E4 Pa·s and $\tau_0 = 1\ \mathrm{N/m^2}$.

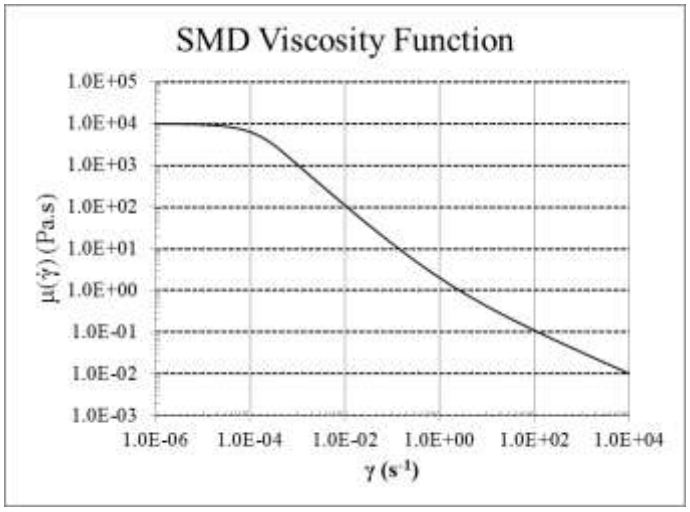

Figure 1 - Plot of the SMD viscosity function for K = 1 Pa·s$^{0.5}$, n = 0.5, $\mu_0 = 1E4$ Pa·s and $\tau_0 = 1$ N/m^2.

De Souza Mendes and Dutra (2004) also propose the following governing parameters for examination of the viscoplasticity and flow inertia effects separately: the power-law coefficient *n*, the rheological Reynolds number defined as

$$Re_r \equiv \frac{\rho L_c^2}{2K\dot{\gamma}_1^{n-2}} \tag{14}$$

where $\dot{\gamma}_1 \equiv (\frac{\tau_0}{K})^{1/n}$ and L_c is a characteristic length, the dimensionless Jump number defined as

$$J \equiv \frac{\rho L_c^2}{2K\dot{\gamma}_1^{n-2}} \tag{15}$$

and the dimensionless velocity U^*, computed as

$$U^* = \frac{U_c}{\dot{\gamma}_1 L_c}. \tag{16}$$

In Eq. (16), U_c is the characteristic speed. The rheological Reynolds number may be interpreted as a dimensionless density based only on the liquid's rheological properties (Dall'Onder dos Santos et al., 2010). The Jump number provides the relative measure of the shear rate jump when the shear stress reaches the yield value τ_0. For $U^* \ll 1$, the liquid behaves as a very high viscosity Newtonian liquid. For $U^* \cong 1$ and higher, the liquid transitions to a power-law like governed liquid. The power-law Reynolds number, Eq. (17), gives the ratio of inertia forces relative to viscous forces:

$$Re \equiv \frac{\rho U_c^{2-n} L_c^n}{K}. \tag{17}$$

In order to examine the inertia and turbulence effects for the same viscoplasticity, the power-law Reynolds number raises while keeping constant the power-law coefficient *n*, the rheological Reynolds number and the Jump number.

3. NUMERICAL METHODOLOGY

The Finite Volume Method, as implemented by the commercial software Star-CCM+ (CD-Adapco, 2012), numerically approximates the transport equations for mass, momentum, turbulence kinetic energy, turbulence dissipation rate, normal stress and elliptic functions for constant density. The SMD viscosity function evaluates the dynamic viscosity. The flow's velocity-pressure coupling computes with the SIMPLE algorithm (Patankar and Spalding, 1972). The Gauss-Seidel method iteratively solves the resulting system of linear equations. Non-slip impermeable walls and a symmetry plane located at z = 0.5 m bound the computational domain. The walls have a characteristic length $L_c = 1$ m and the cavity's lid moves from left to right in the XZ plane at uniform characteristic speed U_c. Hexahedral volumes discretize the computational domain for three mesh refinement levels in order to verify

the numerical result's uncertainty and mesh dependency, following the generalized Richardson's Extrapolation Method (Roache, 1998). The meshes' design adopts well-known guidelines (Mavriplis et al., 2009) and aims to obtain $y^+ \cong 0.5$ across the first layer of volumes bounding the lid wall, considering the flow as turbulent for the characteristic length and lid speed, the viscosity taken as μ_0. As U^* approaches the unity, the dynamic viscosity decreases by the Jump number's magnitude and the actual y^+ value severely departs from its design value. Table 1 summarizes the parameters used to generate the set of meshes:

Table 1 – Parameters for generating the set of meshes.

L_c (m)	U_c (m/s)	Re	y+	B.L. ratio	B.L. Nodes	$\delta_{B.L.}$ (m)	Δs_1 (m)	r_{ref}
1.0	1.5874	2500	0.50	1.1	12	8.4267E-02	4.5473E-03	1.4422

In Tab. 1, B.L. ratio is the growth ratio of the volumes within the flow's boundary layer, estimated to be $\delta_{B.L.}$ meters height and having B.L. Nodes spanning the lid's normal direction. To achieve the design y^+ value for the power-law Reynolds number Re = 2500 and the characteristic length and lid speed, the first volume height across the lid wall is Δs_1 meters, the same value adopted for the remaining walls of the cavity for easier mesh generation and symmetry reasons. The Δs_1 value also determines the node clustering near the cavity's vertexes and the hyperbolic node distribution along the edges (Vinokur, 1980). The ratio of the number of volumes between each increasing mesh refinement level, being N3 the coarsest, N2 the intermediate and NI the finest mesh, is approximately the cube of the refinement ratio r_{ref}. Table 2 summarizes the mesh set characteristics and the rheological parameters used in all simulations, including the verification cases.

Table 2 – The mesh set characteristics and the rheological parameters used in all simulations.

Mesh	Nodes (x, y, z)	Volumes	ρ (kg/m3)	K (Pa.s^n)	n	μ_0 (Pa·s)	τ_0 (N/m^2)	J	Re_r	U^*
N3	57, 57, 29	94221	1.25E+03	1	0.5	1.0E+04	1	1.0E+04	625	1.5874
N2	83, 83, 41	282449								
N1	121, 121, 61	893101								

Table 3 presents the numerical values for the wall shear stress τ_w probed at (x, y, z) = (0.5, 0.0, 0.5), converged to the steady state and machine precision. In Tab. 3, R.E. is the extrapolated wall shear stress value using N2 and N1 τ_w values. Δ% is the percent ratio between the actual and extrapolated values. The percent grid convergence index (GCI %) provides a measure of uncertainty for a set of three meshes being p the computed order of convergence for that set. The ratio between the GCI% values (r_{GCI}) and the p-nth power of the refinement ratio r_{ref} indicate how close to the asymptotic convergence region the mesh set is situated. The r_{GCI}/r_{ref}^p ratio value close to the unity indicates that N3, N2 and N1 are a valid, verifiable set of meshes. The results presented in the following section make selective use of the meshes as the power-law Reynolds number is increased and the calculation residuals indicate that a finer mesh would produce data that are more accurate.

Table 3 – The values for the wall shear stress τ_w probed at (x, y, z) = (0.5, 0.0, 0.5).

Mesh	τ_w (N/m^2)	Δ%	GCI %	R.E.	p	r_{GCI}/r_{ref}^p
N3	4.1816	0.09	-	4.1777	3.7428	0.9998
N2	4.1787	0.02	0.03			
N1	4.1779	0.01	0.01			

4. RESULTS

For power-law Reynolds numbers ranging from the unity to 100, the flows simulate as laminar and the liquid is mostly unyielded and stagnant at the bottom region of the cavity. Very close to the sliding lid, the flow field rotates with nearly rigid body motion around the axis line that defines the vortex core, located near the cavity's middle section in the YZ plane. For power-law Reynolds numbers ranging from 500 to 35000, the flows simulate as turbulent. It is worth noting that solution convergence is achievable considering the flows as being laminar but the calculation residuals for momentum and continuity are nearly five orders of magnitude higher than the matching cases simulated as turbulent. It indicates that the laminar solution is not viable or transitional for power-law Reynolds numbers higher than 500. In all figures to follow, the half cavity's symmetry boundary is in first plane and the lid slides from left to right.

Figure 2 depicts the morphology of unyielded regions for laminar flows, where the power-law Reynolds numbers ranges from the unity to 100. Those regions are represented by the strain-rate iso-surfaces where $\dot{\gamma} \leq \tau_0/\mu_0$ (i.e., $\dot{\gamma} \leq$ 1E-4 s^{-1}). The unyielded surfaces tend to vanish and the stagnant regions tend to shrink as the power-law Reynolds increases.

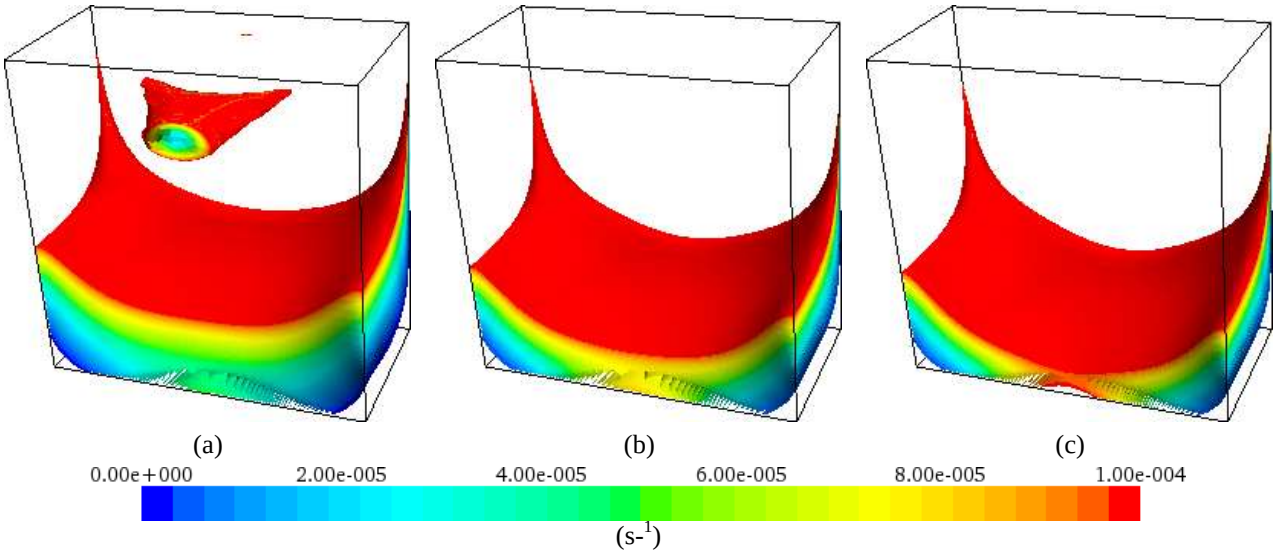

Figure 2 – Strain-rate iso-surfaces, where $\dot{\gamma} \leq \tau_0/\mu_0$ (i.e., $\dot{\gamma} \leq$ 1E-4 s^{-1}) for Re =1 (a), Re = 25 (b) and Re = 100 (c).

Figure 3 illustrates the vorticity iso-surfaces for power-law Reynolds numbers ranging from the unity to 100 where the Q Criterion, defined as $Q \equiv 1/2\,(|\mathbf{\Omega}|^2 - |\mathbf{S}|^2)$, is positive. In the preceding equation, $\mathbf{\Omega} = 1/2\,(\nabla\mathbf{u} - \nabla\mathbf{u}^T)$ is the vorticity tensor, positive Q values indicating the regions of the flow that are vorticity-dominated as opposed to strain-dominated. The increase of the power-law Reynolds number causes the strained region near the middle of the lid to move right towards the rear wall.

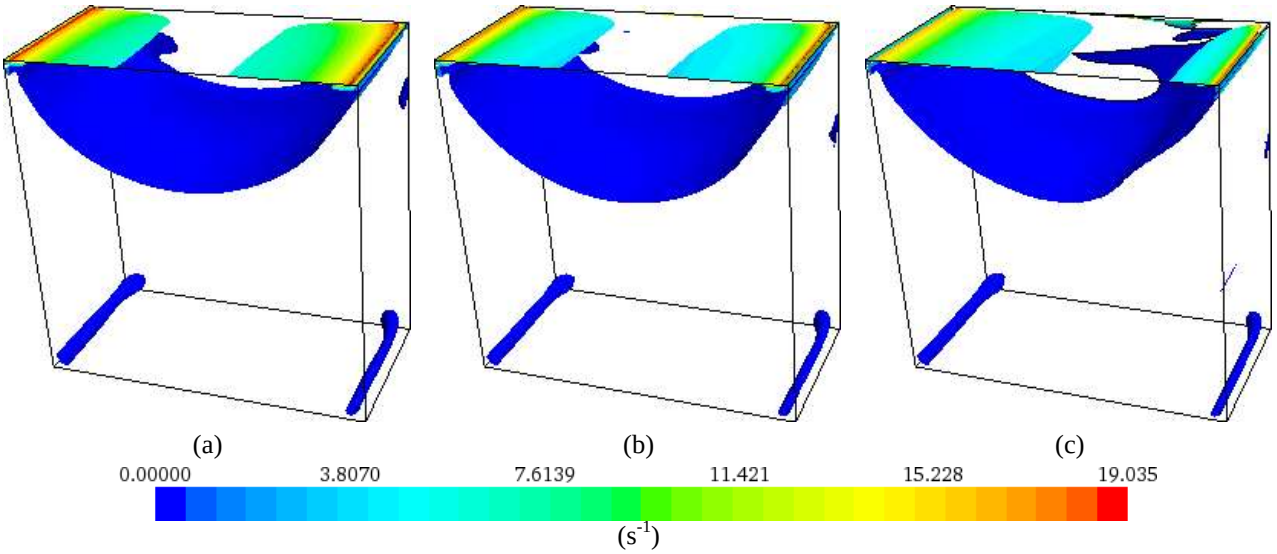

Figure 3 – Vorticity magnitude iso-surfaces for Re =1 (a), Re = 25 (b) and Re = 100 (c).

Figure 4 pictures the vorticity magnitude of the flow streamlines for power-law Reynolds numbers ranging from the unity to 100. The position of the axis line around which the flow field rotates, the vortex core, computes as proposed by Sujudi and Haimes (1995). The vortex core is nearly perpendicular to the flow and the vortexes are planar and not stretched. As the power-law number rises, the vortexes enlarge and stretch from inside out towards the sidewalls. The vortex core shifts its position forward and begins to curve.

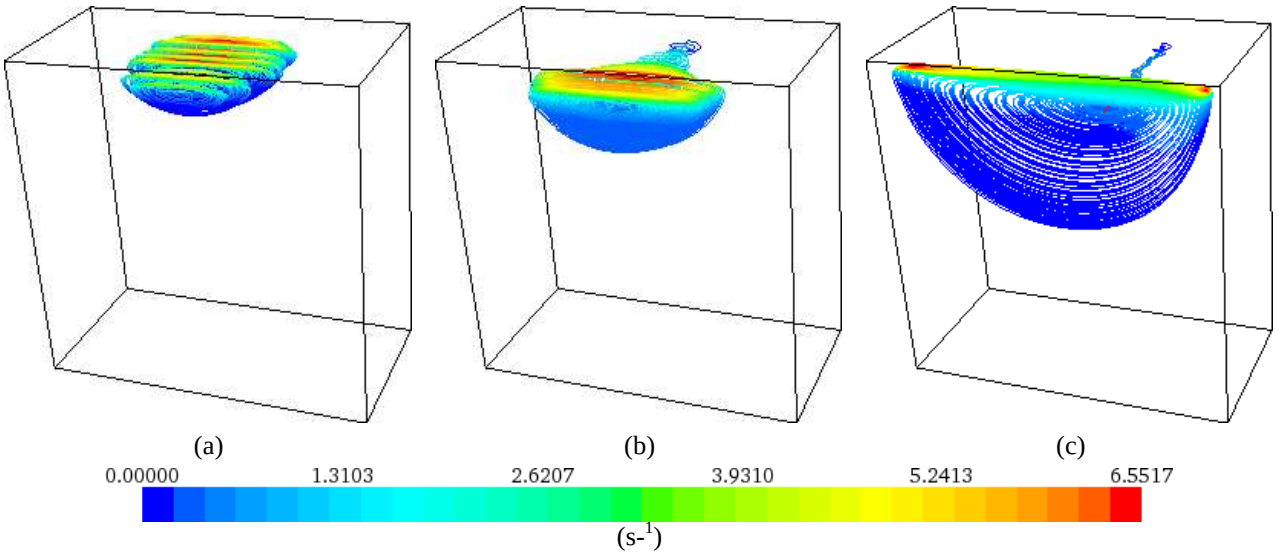

Figure 4 – Vorticity magnitude of the flow streamlines for Re =1 (a), Re = 25 (b) and Re = 100 (c).

For the turbulent power-law Reynolds numbers ranging between 500 and 35000, the unyielded surfaces tend to confine to the lower edges and to the corners of the cavity as shown in Fig. 5. In Fig. 6, the vortexes begin to stretch and to detach from the walls, deforming the vorticity iso-surfaces. The flow streamlines depart from the regular pattern to follow the vortex stretching associated to turbulent flows in Fig. 7. For the power-law Reynolds numbers Re = 20000 and Re = 35000, the unyielded surfaces are barely noticeable. The vorticity iso-surfaces, pictured in Fig. 8, show strong vortex shedding and flow detachment from the walls. The vortex cores originate in different regions of the flow as seen in Fig. 9, where the vortex-stretching phenomenon prevails.

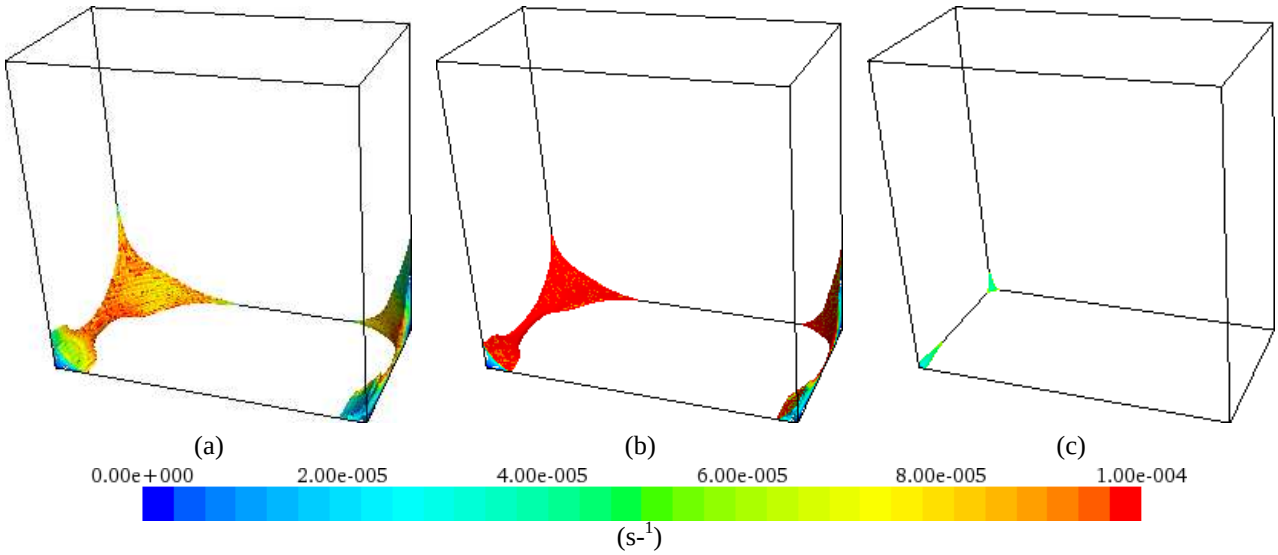

Figure 5 – Strain-rate iso-surfaces where $\dot{\gamma} \leq$ 1E-4 s^{-1} for Re =500 (a), Re = 2500 (b) and Re = 10000 (c).

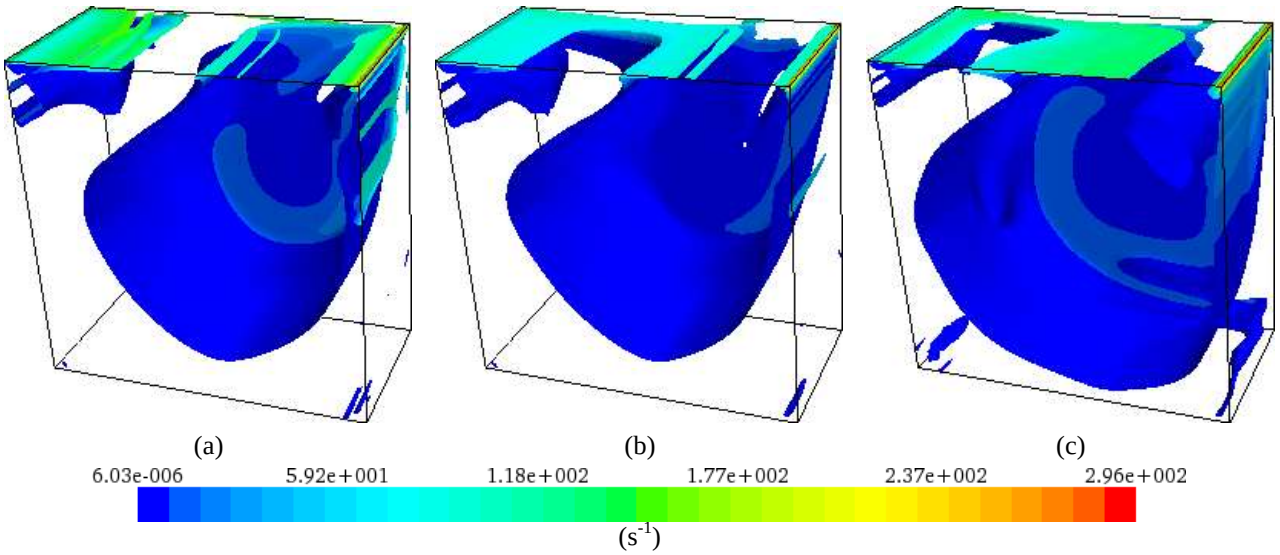

Figure 6 – Vorticity magnitude iso-surfaces for Re =500 (a), Re = 2500 (b) and Re = 10000 (c).

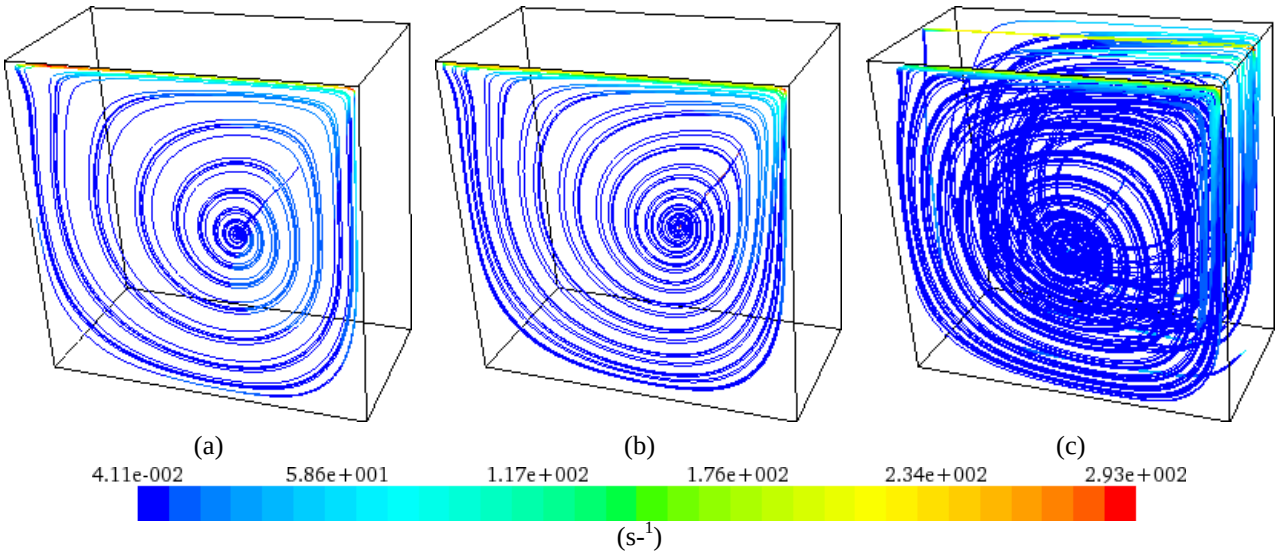

Figure 7 – Vorticity magnitude of the flow streamlines for Re =500 (a), Re = 2500 (b) and Re = 10000 (c).

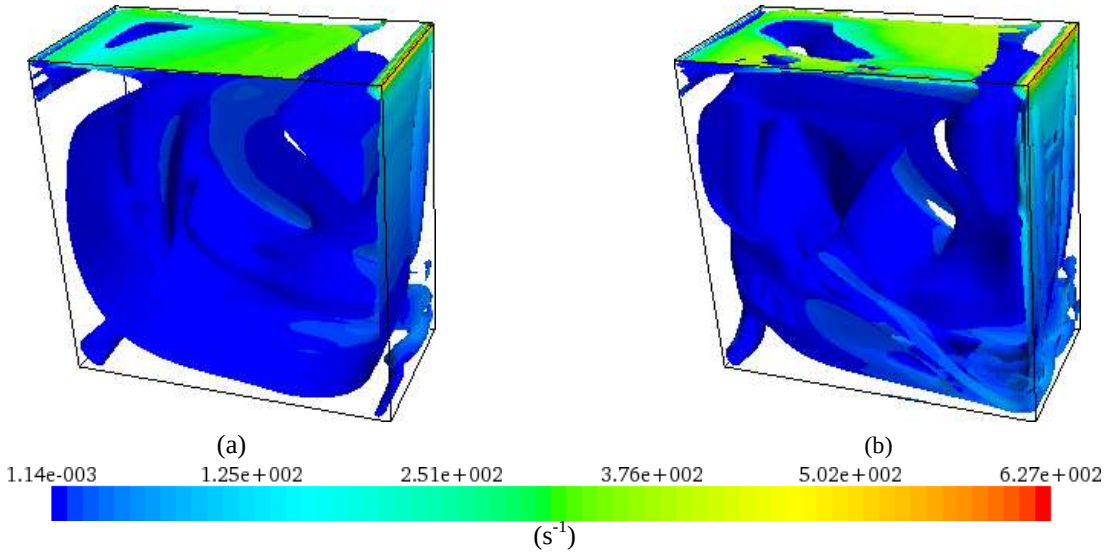

Figure 8 – Vorticity magnitude iso-surfaces for Re =20000 (a), Re = 35000 (b).

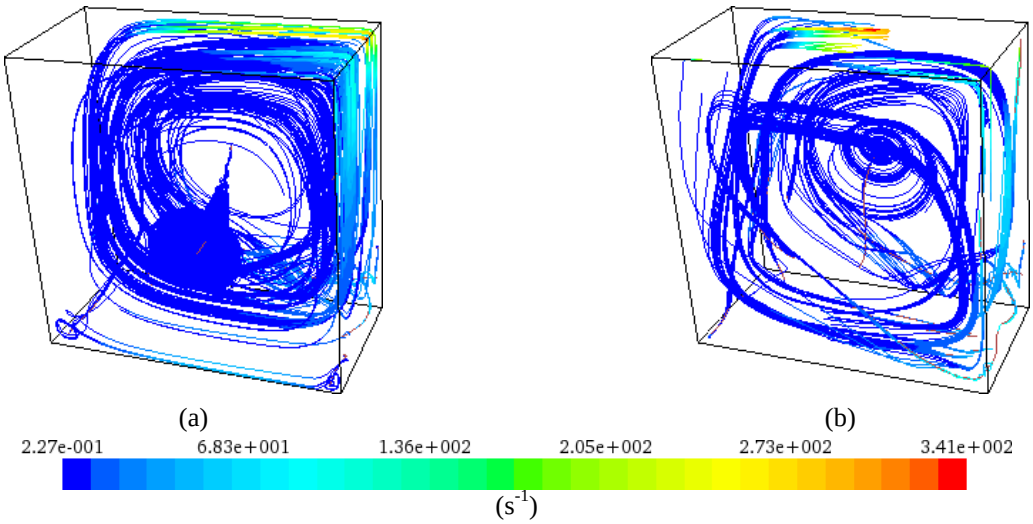

Figure 9 – Vorticity magnitude of the flow streamlines for Re =20000 (a), Re = 35000 (b).

5. CONCLUSIONS

The coupling of the SMD viscosity function and the V2F turbulence model presented consistent results from both the rheological and turbulence perspectives. The ability of the turbulence model to handle low and high y^+ values without resourcing to wall functions is of utmost importance to get accurate results. The formulation of the SMD viscosity function allows the examination of the inertia and turbulence effects for the same viscoplasticity. The results for higher power-law Reynolds number showed strong vortex shedding and vortex stretching, characteristics of turbulent flows.

6. ACKNOWLEDGMENTS

The authors thank CNPq and CAPES (P.A. Beck graduate scholarship) for the financial support.

7. REFERENCES

CD-adapco, 2012. User Guide Star-CCM+ 6.06.17, pp. 4347-4383.

Dall'Onder dos Santos, D., Frey, S.L., Naccache, M.F., de Souza Mendes, P.R., 2010. "Numerical Approximations for SMD in a Lid-Driven Cavity", Pre-print.

de Souza Mendes, P.R., Dutra, E.S.S., 2004. "Viscosity Function for Yield Stress Liquids". Applied Rheology, Vol. 14, Issue 6, pp. 296-302.

Durbin, P.A., 1995. "Separated Flow Computations with the k-ε-υ^2 Model", AIAA Journal, Vol. 33, No. 4, April 1995, pp. 659-664.

Jones,W.P., Launder, B.E., 1972. "The Prediction of Laminarization with a Two-Equation Model of Turbulence", Int. J. Heat and Mass Transfer, Vol. 15, pp. 301-314.

Mavriplis, D.J., Vassberg, J.C., Tinoco, E.N., Mani, M., Brodersen, O.P., Eisfeld, B., Wahls, R.A., Morrison, J.H., Zickuhr, T., Levy, D., Murayama, M., 2009. "Grid Quality and Resolution Issues from the Drag Prediction Workshop Series", Journal of Aircraft, Vol. 46, No. 3.

Patankar, S.V., Spalding, D.B., 1972. "A Calculation Procedure for Heat, Mass and Momentum Transfer in Three-Dimensional Parabolic Flows", Int. J. Heat Mass Transfer, Vol. 15, p. 1787.

Roache, P.J., 1998. "Verification and Validation in Computational Science and Engineering", Hermosa Publishers.

Sujudi, D., Haimes, R., 1995. "Identification of swirling flow in 3-D vector fields", AIAA 12th Computational Fluid Dynamics Conference, Paper 95-1715.

Vinokur, M., 1980. "On One-Dimensional Stretching Functions for Finite-Difference Calculations", NASA CR 3313.